Nonlinear dynamics of a backward quasi-phase-matched second-harmonic generator

G. D'Alessandro,[1] P. St. J. Russell,[2] and A. A. Wheeler[1]
[1]*Department of Mathematics, University of Southampton, Southampton, SO17 1BJ, United Kingdom*
[2]*School of Physics, University of Bath, Claverton Down, Bath BA2 7AY, United Kingdom*
(Received 6 December 1996)

We study the stability of the interaction between a pump wave and a counter propagating second-harmonic wave phase-matched in a periodically poled $\chi^{(2)}$ material using both analytical and numerical methods. In contrast to the more usual copropagating case, backward phase-matched frequency doubling displays richer and more complex behavior, owing to the presence of built-in feedback. [S1050-2947(97)08104-3]

PACS number(s): 42.65.Ky, 42.79.Nv, 42.65.Sf

I. INTRODUCTION

The recent high level of interest in $\chi^{(2)}$ phenomena is due largely to dramatic improvements in the fabrication of periodically poled materials (both crystals and glasses) for quasi-phase-matching [1–3]. By relaxing the requirement for birefringence phase-matching, quasi-phase-matching allows the use of any nonlinear crystal or glass, provided it can be periodically poled at the correct pitch. This is making possible efficient frequency doubling of near infrared diode lasers into the blue, and parametric generation of tunable radiation at communications and gas sensing wavelengths beyond $1\,\mu$m [4]. It is also significant for experiments on the ''cascaded'' nonlinear phase phenomenon [5], which yields nonlinear phase changes that can greatly exceed those available in $\chi^{(3)}$ materials.

In ''cascading'' the down-conversion of second-harmonic light is accompanied by a nonlinear change in the phase of the fundamental wave. At perfect phase-matching, down-conversion does not occur (ignoring parametric amplification of vacuum photons). In order to observe the cascaded nonlinearity, therefore, a phase mismatch is required under normal copropagating conditions, since some second-harmonic light must be generated before down-conversion can proceed. If, however, a second-harmonic wave is injected with an appropriate phase relative to the fundamental wave, down-conversion will occur, resulting in a phase-change in the fundamental wave. Indeed, this process is most effective at exact phase-matching [10].

This becomes important in the presence of feedback, for example if second-harmonic light is fed back to the input of a frequency doubling system, when nonlinear phase effects clearly become possible. Consider, for example, a ring cavity singly resonant at the second harmonic and pumped by the fundamental wave (Fig. 1). Under these circumstances, second-harmonic light is present at the input of the doubler. Since its intensity depends on the fundamental power, this can give rise to nonlinear phase changes in the fundamental wave. Furthermore, not only the amplitude but also the phase of the feedback second harmonic depends on the pump power. This means that the system will behave in a highly complex manner as a function of input power, since the direction of the conversion depends on the relative phase between second harmonic and fundamental [6,7].

It is the aim of this paper to study and analyze the stability of another doubling system with built-in feedback: a backward frequency doubler in which quasi-phase-matching is achieved by small pitch periodic poling. In distributed feedback frequency doubling, backward phase matching is achieved when the quasi-phase-matching pitch is of order $\lambda_{SH}/2n_{SH}$, where n_{SH} is the refractive index at the second-harmonic wavelength λ_{SH}. For conversion between 1.55 and 0.775 μm in lithium niobate, this works out at around 180 nm, which is beyond the current capabilities of electric field poling techniques. Noting that the pitch rises in proportion to the order of the Bragg condition, Risk *et al.* [8] have recently fabricated a third order Bragg reflector in KTP using ion exchange (0.7-μm pitch). An odd-valued higher order quasi-phase-matching condition could be used for backward quasi-phase-matching. In lithium niobate, for example, the ninth-order condition would require a pitch of 1.6 μm, which should be within reach using current techniques.

The continuous-wave properties of this system can be modeled by a system of two coupled partial differential equations (7) and (8). The steady form of these equations, for both the copropagating and counterpropagating cases, has been studied by Russell [9,10], who derived the Hamiltonian and found solutions expressed in terms of Jacobian elliptic functions. More recently, Trillo and Wabnitz [11,12] studied the copropagating case and used its Hamiltonian structure to characterize the solutions. In this paper, we characterize the properties of a backward phase-matched frequency doubling system from the Hamiltonian structure of its equations, and analyze the temporal dynamics and stability of the solutions. We find that the backward phase-matched system displays

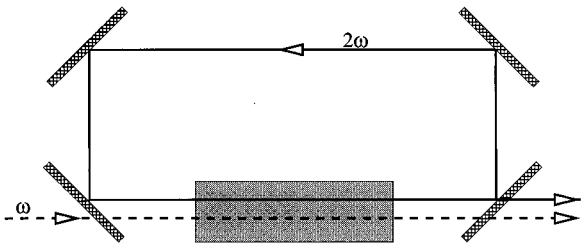

FIG. 1. Nonlinear interaction of a pump and a second-harmonic beam in a $\chi^{(2)}$ material. The feedback induced by the cavity, singly resonant at the second harmonic, can induce a very rich dynamical behavior.

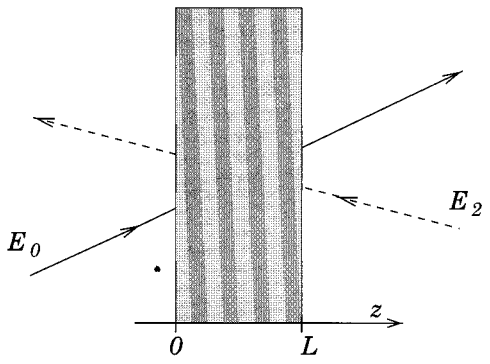

FIG. 2. Schematic diagram of the model. Two beams, E_0 and E_2, counterpropagate through the nonlinear crystal where they are coupled by the modulated nonlinear susceptibility, $\chi^{(2)}$.

stationary solutions that undergo Hopf bifurcation to self-pulsing solutions as the input intensity is increased.

In the next section we describe the system and derive the nondimensional governing equations. We then go on to consider the steady solutions and employ Hamiltonian techniques to provide a qualitative description of the solution structure and the role of the phase mismatch. Further, we use the method of matched asymptotic expansions to give approximate solutions when the ratio of the second-harmonic input intensity to the pump input intensity is small. In Sec. IV we consider the time dependent problem. We employ a spectral representation of the solutions allied to numerical continuation to study numerically the bifurcation structure and the nature of the time dependent solutions. We find that for low input powers there is a stable steady solution. This undergoes a series of Hopf bifurcations to a pulsed output as the input power is increased.

II. THE CONFIGURATION

We consider two plane waves, of frequency ω and 2ω counterpropagating through a periodically poled $\chi^{(2)}$ material; see Fig. 2. We neglect polarization effects and so may express the electric fields of the two waves as

$$E_0=\frac{1}{2}\mathcal{E}_0(z,t)\exp[i(\boldsymbol{k}_0\cdot\boldsymbol{r}-\omega t)]+\text{ c.c.}, \tag{1}$$

$$E_2=\frac{1}{2}\mathcal{E}_2(z,t)\exp[i(\boldsymbol{k}_2\cdot\boldsymbol{r}-2\omega t)]+\text{c.c.} \tag{2}$$

Here $\mathcal{E}_0(z,t),\mathcal{E}_2(z,t)$ represent the slowly varying complex amplitudes and $\boldsymbol{k}_0,\boldsymbol{k}_2$ the wave vectors of the forward and backward waves, respectively. We assume that the material is periodically poled and that the nonlinear susceptibility is of the form

$$\chi^{(2)}=\frac{\chi_m}{2}\exp[i\boldsymbol{k}_m\cdot\boldsymbol{r}]+\text{ c.c.}, \tag{3}$$

where $\boldsymbol{k}_m$ is the wave vector of the modulation and we assume that χ_m is a real quantity. The wave vectors $\boldsymbol{k}_0$ and $\boldsymbol{k}_2$ are chosen so that

$$\boldsymbol{k}_2=2\boldsymbol{k}_0-\boldsymbol{k}_m. \tag{4}$$

Inserting these forms into the Maxwell wave equation and making use of the slowly varying amplitude approximation we obtain two equations coupling the two amplitudes $\mathcal{E}_0$ and $\mathcal{E}_2$:

$$[1+\chi(\omega)]\frac{2i\omega}{c^2}\frac{\partial\mathcal{E}_0}{\partial t}+2i(\boldsymbol{k}_0\cdot\boldsymbol{e}_z)\frac{\partial\mathcal{E}_0}{\partial z}=-\frac{\omega^2\chi_m}{2c^2}\mathcal{E}_0^*\mathcal{E}_2, \tag{5}$$

$$[1+\chi(2\omega)]\frac{4i\omega}{c^2}\frac{\partial\mathcal{E}_2}{\partial t}+2i(\boldsymbol{k}_2\cdot\boldsymbol{e}_z)\frac{\partial\mathcal{E}_2}{\partial z}$$
$$=-\frac{\omega^2\chi_m}{c^2}\mathcal{E}_0^2-\left\{\frac{4\omega^2}{c^2}[1+\chi(2\omega)]-|\boldsymbol{k}_2|^2\right\}\mathcal{E}_2, \tag{6}$$

where we have assumed that dispersion and diffraction are negligible. Here $\chi(\omega)$ is the linear susceptibility of the material, c is the speed of light *in vacuo*, and the superscript star represents the complex conjugate. The nondimensional form of these equations may be expressed as

$$(\partial_\tau+\partial_\zeta)a=ba^*, \tag{7}$$

$$(\partial_\tau-\gamma\partial_\zeta)b=-a^2+i\vartheta b, \tag{8}$$

where dimensionless time τ and distance ζ are defined by

$$\tau=\left[\frac{v(\omega)}{Lk_0}(\boldsymbol{k}_0\cdot\boldsymbol{e}_z)\right]t,\quad \zeta=\frac{z}{L}, \tag{9}$$

respectively. Here L is the crystal thickness (see Fig. 2), $v(\omega)$ is the phase velocity of a wave of frequency ω, $\boldsymbol{e}_z$ is the unit vector in the z direction, and k_i denotes $|\boldsymbol{k}_i|$, $i=0,2$. Under this scaling the interior of the crystal is represented by $0\leqslant\zeta\leqslant1$ and one unit of dimensionless time corresponds to the time taken by the pump beam to traverse the crystal. The relative phase velocity of the two fields is

$$\gamma=-\frac{1}{2}\frac{v^2(2\omega)}{v^2(\omega)}\frac{\boldsymbol{k}_2\cdot\boldsymbol{e}_z}{\boldsymbol{k}_0\cdot\boldsymbol{e}_z} \tag{10}$$

and the phase mismatch parameter is

$$\vartheta=\frac{v^2(2\omega)}{v^2(\omega)}\frac{(\omega^2/c^2)[1+\chi(2\omega)]-|\boldsymbol{k}_2|^2}{4(\boldsymbol{k}_0\cdot\boldsymbol{e}_z)}L. \tag{11}$$

Note that, since $v(2\omega)\simeq v(\omega)$, γ is approximately 1 for counterpropagating geometries. Finally, the dimensionless forms of the complex electric fields are

$$a=\frac{v(2\omega)}{v(\omega)}\frac{L\omega^2\chi_m}{4c^2(\boldsymbol{k}_0\cdot\boldsymbol{e}_z)}\mathcal{E}_0,\quad b=i\frac{L\omega^2\chi_m}{4c^2(\boldsymbol{k}_0\cdot\boldsymbol{e}_z)}\mathcal{E}_2. \tag{12}$$

As a natural consequence of the configuration the waves are specified on input to the medium. We note that the governing equations are invariant under a constant phase shift of both waves and so we may, without loss of generality, set the phase of $a(0,t)$ to zero. In light of this we will subject the governing equations (7) and (8) to the following boundary conditions:

$$a(0,t)=A_0\quad\text{and}\quad b(1,t)=B_0\exp(i\beta_0), \tag{13}$$

where A_0 and B_0 are the input moduli of the forward and backward fields, respectively, and β_0 is the phase difference between the two waves on input.

III. STATIONARY PROBLEM

A. The effect of phase mismatch

We now consider the time independent solutions of Eqs. (7) and (8) and the associated boundary conditions (13) which satisfy the ordinary differential equations

$$a' = ba^*, \tag{14}$$

$$b' = a^2 - i\vartheta b, \tag{15}$$

where the prime denotes differentiation with respect to ζ. Without loss of generality we have set $\gamma = 1$ [if $\gamma \neq 1$ a and ϑ may be rescaled with γ to put the equations in the form of Eqs. (14) and (15)]. It may be shown that, as a consequence of conservation of energy, the energy flux

$$\mathcal{D} = |a|^2 - |b|^2 \tag{16}$$

is constant throughout the crystal. We now write

$$a = A\exp(i\alpha) \quad \text{and} \quad b = B\exp(i\beta), \tag{17}$$

where A,B and α,β represent the moduli and phases of the two fields, respectively. The governing equations become

$$\begin{aligned} A' &= AB\cos(\phi), \quad B' = A^2\cos(\phi), \\ \alpha' &= B\sin(\phi), \quad \beta' = -\frac{A^2}{B}\sin(\phi) - \vartheta, \end{aligned} \tag{18}$$

where $\phi = \beta - 2\alpha$. Using the conservation law (16) we may recast these equations as

$$B' = (\mathcal{D} + B^2)\cos(\phi), \quad \phi' = -\left(\frac{\mathcal{D} + 3B^2}{B}\right)\sin(\phi) - \vartheta. \tag{19}$$

A quantitative study of these equations is precluded as the boundary condition for ϕ cannot be deduced from Eq. (13). Nevertheless, a qualitative study may be conducted by expressing them in Hamiltonian form [9,11,12]:

$$q' = \frac{\partial \mathcal{H}}{\partial p}, \quad p' = -\frac{\partial \mathcal{H}}{\partial q}, \tag{20}$$

where $p = \phi$, $q = B^2$ and the Hamiltonian is given by

$$\mathcal{H} = 2\sqrt{q}(\mathcal{D} + q)\sin(p) + \vartheta q, \tag{21}$$

and therefore the quantities $\mathcal{D}$ and $\mathcal{H}$ are conserved, i.e., independent of position. We exploit this to understand the solution structure by plotting the level sets of $\mathcal{H}$ in (q,p) space for fixed values of $\mathcal{D}$ and the phase mismatch ϑ, see Fig. 3. The abscissa is q and the ordinate is p. We note from the definition of the Hamiltonian that its level sets are 2π periodic with respect to p and hence the range of the ordinate is 2π. We have only plotted examples of ϑ positive because of the property $\mathcal{H} \to -\mathcal{H}$ if $p, \vartheta \to -p, -\vartheta$.

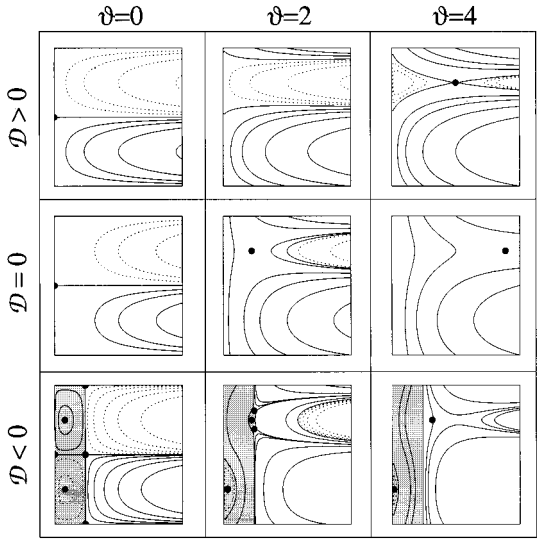

FIG. 3. Each plot shows the contours of the Hamiltonian given by Eq. (21) in (q,p) space; solid and dashed curves represent $\mathcal{H}$ positive and negative, respectively. The ordinate is p and it ranges from 0 to 2π, the abscissa is q and it ranges from 0 to 2 in all plots except the three cases for which $\mathcal{D}<0$, where it ranges from 0 to 5. The solid dots indicate the nonlinear eigenmodes. The shaded areas represent regions of (q,p) space that are not physically accessible ($q \leqslant -\mathcal{D}$).

In Fig. 3 closed contours (including those which are 2π periodic with respect to p) correspond to solutions in which the magnitudes $|a(\zeta)|$ and $|b(\zeta)|$ are periodic in space, as energy is repeatedly exchanged between the two fields. In contrast, the phases α and β are not generally 2π-periodic, see Fig. 4. Henceforth we will refer to such solutions as ''spatially oscillatory.'' We also observe from this figure and Eq. (18) that β and hence ϕ undergo a rapid change when the magnitude of b is small. We will exploit this property in Sec. III B below to find an approximate solution.

We now consider in detail the phase matched situation, $\vartheta = 0$, illustrated in Fig. 3. The case $\mathcal{D}<0$ appears qualitatively different to the cases $\mathcal{D}=0$ and $\mathcal{D}>0$, because of the presence of closed contours. It may be shown from the definition of $\mathcal{H}$, Eq. (21), that the closed contours exist for $q < -\mathcal{D}$, which is in contradiction to the definition of $\mathcal{D}$, Eq. (16), which implies $q \geqslant -\mathcal{D}$, and so they are not physically realizable. We thus deduce that for zero phase mismatch there are no spatially oscillatory solutions. Therefore the only possible solutions have at most one minimum in q, the intensity of the backward field, and hence in the intensity of the forward field as well (because $\mathcal{D}$ is fixed).

In contrast, for nonzero phase mismatch spatially oscillatory solutions are possible. The geometry of the level sets of $\mathcal{H}$ is organized by its saddle points. In particular, they control the existence of closed contours; there are spatially oscillatory solutions only if there is a saddle point. The saddle points are sometimes termed ''nonlinear eigenmodes'' [9,13] and represent solutions in which the two waves propagate through the crystal with constant amplitude as if they are not interacting. From Eq. (21) there is a pair of saddle points when $\mathcal{D}<0$ and $|\vartheta| \leqslant 2\sqrt{-\mathcal{D}}$, for which $q = -\mathcal{D}$. They correspond to a mode of operation where the pump field is zero

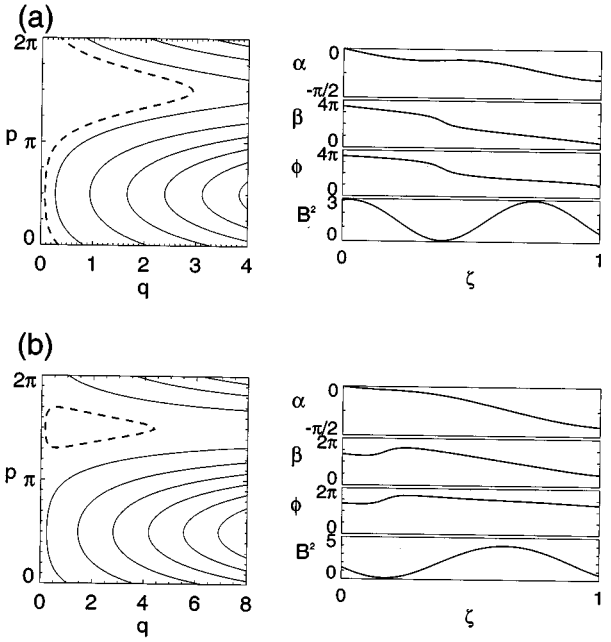

FIG. 4. Examples of spatially oscillatory solutions. Each contour plot shows the level sets of the Hamiltonian in (q,p) space. The dashed line is the contour of the solution shown in the adjacent right-hand plots. The parameter values for both sets of plots are $B_0=0.8$, $\beta_0=\pi/2$, $\vartheta=12$ but in (a) $A_0=3$ while in (b) $A_0=3.305$.

and the higher frequency field, b, propagates unaltered through the crystal. In addition there are more physically interesting saddle points at

$$\sqrt{q}=\frac{1}{6}[-\vartheta\pm\sqrt{\vartheta^2-12\mathcal{D}}],\quad p=\frac{\pi}{2}, \tag{22}$$

$$\sqrt{q}=\frac{1}{6}[+\vartheta\pm\sqrt{\vartheta^2-12\mathcal{D}}],\quad p=\frac{3\pi}{2}. \tag{23}$$

As $\sqrt{q}$ is real and positive, it follows that if $\mathcal{D}\leqslant 0$ spatially oscillatory solutions exist for all $\vartheta\neq 0$, whereas for $\mathcal{D}>0$ they only exist $|\vartheta|>2\sqrt{3\mathcal{D}}$. However, as discussed above for the case $\vartheta=0$, spatially oscillatory solutions are only physically realizable if $q\geqslant-\mathcal{D}$, which for negative $\mathcal{D}$ is equivalent to $|\vartheta|\geqslant 2\sqrt{-\mathcal{D}}$. Therefore, for all nonzero $\mathcal{D}$ physically realizable spatially oscillatory solutions only exist for sufficiently large values of the phase mismatch. This behavior is confirmed in Fig. 3.

B. The phase-matched case

The Hamiltonian formulation discussed above provides a powerful vehicle for describing the qualitative nature of the stationary solutions. We now seek a more quantitative representation of these solutions and to this end we henceforth study the equations in the perfectly phase-matched case, $\vartheta=0$, which is the most physically relevant situation.

In this subsection we employ the method of matched asymptotic expansions [14,15] in the limit $B_0/A_0\to 0$, which corresponds to the configuration where this device is used for second-harmonic generation. We note from the governing equations (18) and Fig. 4 that when B/A is small β varies rapidly, which suggests the presence of a *thin* region (termed a ''boundary layer'' or ''inner region'') in the crystal adjacent to the end $\zeta=1$, where β varies significantly from its input value. The method of matched asymptotic expansions represents the solution as two perturbation expansions in a small parameter proportional to B_0/A_0: one in the boundary layer (the ''inner expansion'') and one outside it (the ''outer expansion''). These expansions are then matched together in order to satisfy the boundary conditions.

It is convenient to introduce the notation $\epsilon=B_0$ and we will seek the solution of Eq. (18) in the limit $\epsilon\to 0$ with $\vartheta=0$ and $A_0=O(1)$:

$$\begin{aligned} A'&=AB\cos(\beta-2\alpha),\quad B'=A^2\cos(\beta-2\alpha),\\ \alpha'&=B\sin(\beta-2\alpha),\quad \beta'=-\frac{A^2}{B}\sin(\beta-2\alpha), \end{aligned} \tag{24}$$

with boundary conditions

$$A(0)=A_0,\quad \alpha(0)=0,\quad B(1)=\epsilon,\quad \beta(1)=\beta_0. \tag{25}$$

1. The inner expansion

The boundary layer width and the backward field are both $O(\epsilon)$. Hence we write

$$\begin{aligned} A&=\hat{A}(\xi)+O(\epsilon),\quad B=\epsilon\hat{B}(\xi)+O(\epsilon^2),\\ \alpha&=\hat{\alpha}(\xi)+O(\epsilon),\quad \beta=\hat{\beta}(\xi)+O(\epsilon), \end{aligned} \tag{26}$$

where $\xi=(1-\zeta)/\epsilon$ represents distance from the end of the crystal, $\zeta=1$, scaled to the width of the boundary layer, and the caret denotes quantities within the boundary layer. At leading order in ϵ the equations in the boundary layer are

$$\begin{aligned} \hat{A}_\xi&=0,\quad \hat{B}_\xi=\hat{A}^2\cos(\hat{\beta}-2\hat{\alpha}),\\ \hat{\alpha}_\xi&=0,\quad \hat{\beta}_\xi=-\frac{\hat{A}^2}{\hat{B}}\sin(\hat{\beta}-2\hat{\alpha}), \end{aligned} \tag{27}$$

with boundary conditions $\hat{B}(0)=1$, $\hat{\beta}(0)=\beta_0$, which determine two constants of integration. The other two are determined by matching to the solution in the outer region. The leading-order solution is found, after matching, to be

$$\begin{aligned} \hat{A}&=\sqrt{\mathcal{D}},\quad \hat{B}=\sqrt{1\pm 2\mathcal{D}\cos(\beta_0)\xi+\mathcal{D}^2\xi^2},\\ \hat{\alpha}&=0,\quad \hat{\beta}=\arctan\left[\frac{\sin(\beta_0)}{\mathcal{D}\xi\pm\cos(\beta_0)}\right], \end{aligned} \tag{28}$$

where the plus-minus sign refers to $\beta_0\in[\pi,2\pi)$ and $\beta_0\in[0,\pi)$, respectively.

2. The outer expansion

In the outer region the solution is given by a regular perturbation expansion of Eq. (24) in powers of ϵ. At leading order matching with the inner solution requires that $\alpha(\zeta)\to 0$ and $\beta(\zeta)\to 0,\pi$ as $\zeta\to 1$, depending on whether $\mathcal{D}$ is negative or positive, respectively. However, the case

$\mathcal{D}<0$ requires that $A<B$, which is inconsistent with the assumption that $B_0/A_0=\epsilon\ll 1$ and henceforth we restrict our attention to the situation $\mathcal{D}>0$. Consequently from Eq. (24) the phases are constant at leading order, $\alpha=0$ and $\beta=\pi$, and the equations for the leading order amplitudes simplify to

$$A'=-AB, \quad B'=-A^2. \tag{29}$$

Their solutions are

$$A=\sqrt{\mathcal{D}}\sec[\sqrt{\mathcal{D}}(1-\zeta)], \quad B=\sqrt{\mathcal{D}}\tan[\sqrt{\mathcal{D}}(1-\zeta)]. \tag{30}$$

The boundary condition upon A at $\zeta=0$ gives that $\mathcal{D}$ must satisfy

$$\sqrt{\mathcal{D}}\sec(\sqrt{\mathcal{D}})=A_0. \tag{31}$$

We note that for all A_0 there is always a solution with $0<\mathcal{D}<\pi^2/4$. Further, if A_0 is sufficiently large, there are additional solutions with $\mathcal{D}>\pi^2/4$. However, they are not physically realizable because the corresponding amplitudes A and B are singular with an infinite energy density within the crystal [9].

The inner and outer expansions may be combined into a composite expansion that represents the solution throughout the whole crystal. This gives

$$A=\sqrt{\mathcal{D}}\sec[\sqrt{\mathcal{D}}(1-\zeta)]+O(\epsilon), \tag{32}$$

$$B=\sqrt{\mathcal{D}}\tan[\sqrt{\mathcal{D}}(1-\zeta)]-\mathcal{D}(1-\zeta) + \epsilon\sqrt{1\pm 2\mathcal{D}\cos(\beta_0)\frac{(1-\zeta)}{\epsilon}+\left[\mathcal{D}\frac{(1-\zeta)}{\epsilon}\right]^2}+O(\epsilon^2), \tag{33}$$

$$\alpha=O(\epsilon), \tag{34}$$

$$\beta=\pm\arctan\left[\frac{|\sin(\beta_0)|}{\mathcal{D}(1-\zeta)/\epsilon\pm\cos(\beta_0)}\right]+O(\epsilon), \tag{35}$$

where, as before, the plus-minus sign refers to $\beta_0\in[\pi,2\pi)$ and $\beta_0\in[0,\pi)$, respectively.

Figure 5 displays a comparison of the leading order composite expansion for β with the result of a numerical integration of the governing equations (24) for $\epsilon=0.05$. It indicates they are in good agreement and clearly shows the boundary layer structure in β.

We define the conversion efficiency, η, of the device for second-harmonic generation as

$$\eta=B(0)^2/A(0)^2. \tag{36}$$

From the composite expansion of A and B this is given by

$$\eta=\sin^2(\sqrt{\mathcal{D}})+O(\epsilon), \tag{37}$$

which along with Eq. (31) implicitly gives the conversion efficiency as a function of the input intensity of the pump field. In Fig. 6 we plot the leading order conversion efficiency as a function of A_0. We observe that the efficiency of the device increases monotonically with the pump intensity.

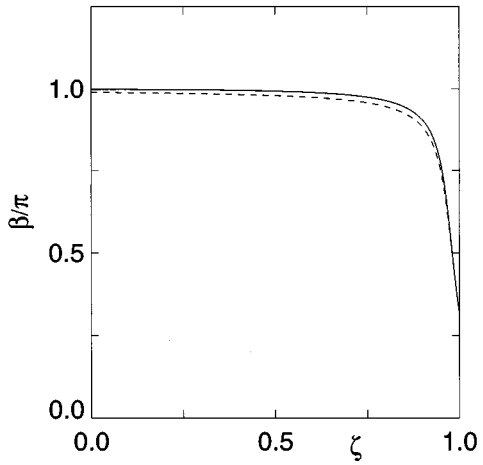

FIG. 5. The solid curve is $\beta(\zeta)$ obtained from a numerical solution of Eq. (24). The dashed curve represents the leading order term in the composite expansion of $\beta(\zeta)$ given by Eq. (35). The parameters are $A_0=3$, $B_0\equiv\epsilon=0.05$, $\beta_0=1$, $\vartheta=0$.

IV. TIME DEPENDENT PROBLEM

In the preceding section we have studied the nature of time stationary solutions. A question that now naturally arises concerns their temporal stability and the related issue of the existence and character of other *time dependent* solutions of the governing equations. To address these questions we now study the fully time dependent equations (7) and (8) using numerical methods based on a Chebyshev spectral technique [16], which we now describe.

The solutions are represented on a nonuniformly spaced (Gauss-Lobatto) grid of $N+1$ points $\zeta_0,\zeta_1,\ldots,\zeta_N$ defined by

$$\zeta_j=\frac{1}{2}\left[1+\cos\left(\frac{\pi j}{N}\right)\right], \quad j=0,\ldots,N, \tag{38}$$

which allows us to easily and accurately calculate the spatial derivative of the solutions by approximating them as a sum of $N+1$ Chebyshev polynomials. In fact the spatial deriva-

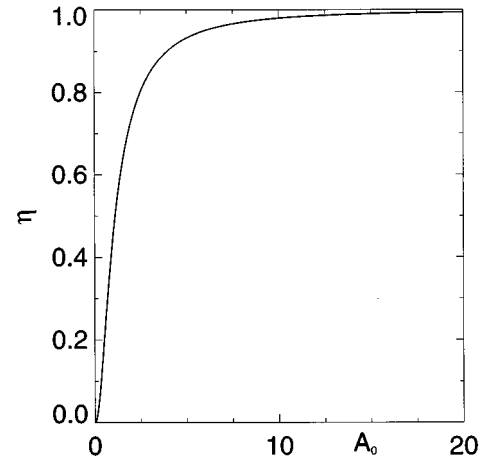

FIG. 6. A plot of the leading order conversion efficiency as a function of the pump intensity given by Eqs. (31) and (37).

tive is given by multiplying the vector comprising values of the solution on the grid by a constant matrix D (whose expression can be found in Ref [16], p. 69). This approximation to the spatial derivative is employed in the governing equations (7) and (8) to obtain a system of nonlinear ordinary differential equations in time for the values of the solution at each grid point:

$$\dot{a}_j = -\sum_{k=0}^{k=N} D_{jk} a_k + b_j a_j^{\star}, \quad \dot{b}_j = \gamma \sum_{k=0}^{k=N} D_{jk} b_k - a_j^2 + i\vartheta b_j,$$

$$j = 0, \ldots, N, \quad (39)$$

where the dot denotes differentiation with respect to time and $a_j = a(\zeta_j), b_j = b(\zeta_j)$. The advantage of using a spectral method over a more standard finite difference method is that spectral methods often exhibit exponential accuracy with the number of grid points. In fact we wrote two codes, one employing the above spectral method and the other an upwind finite difference technique [17], and found that we could obtain the same accuracy between the two by, for example, using 1000 points in the latter and only 20 grid points in the spectral code. It is this feature of the spectral technique that has allowed us to efficiently obtain the results presented below. We have (i) obtained steady solutions as a function of the control parameters A_0, B_0 and β_0, (ii) assessed their linear stability, and (iii) found temporally periodic solutions and investigated their linear stability. All the numerical results given below refer to the situation $\gamma = 1$ and $\vartheta = 0$. We have in fact also done a limited number of computations for other values of γ and ϑ, which suggest that the results given here are qualitatively typical of the behavior of the system.

Steady solutions of Eq. (39) were obtained by using a modified Powell hybrid method, implemented in the SNSQE software [18]. They were compared with the composite expansion obtained from the asymptotic analysis in Sec. III B and shown to be in good agreement (see Fig. 5).

The linear stability of the steady solutions was determined by evaluating the eigenvalues [18] of the Jacobian of the right-hand sides of Eq. (39) evaluated at the steady solution. By monitoring the sign of the real part of the leading eigenvalue we were able to determine the marginal stability surface in (A_0, B_0, β_0) space, see the lower surface in Fig. 7. This indicates that the steady solution loses stability as either A_0 or B_0 are increased and their threshold values strongly depend on the phase difference of the input fields, β_0. We found that on the marginal stability surface the system undergoes a Hopf bifurcation the frequency of which is very weakly dependent on β_0 and B_0. We also found that above the threshold the unstable stationary solution undergoes a further Hopf bifurcation at larger values of A_0 (for given values of β_0 and B_0), see the upper surface in Fig. 7. Over the range of parameters we investigated the two Hopf bifurcations of the steady solution, which occur at distinct values of A_0 and so they are never degenerate. The marginal stability surface has a single minimum with respect to β_0. At $\beta_0 = 0$ and π the system is much more stable (from our calculations we are unable to determine whether the threshold for A_0 is finite at these points). In Fig. 8 we show the intensities of the two fields through the crystal for $\beta_0 = \pi$. We observe that throughout a large part of the crystal the pump beam is essentially zero so that the interaction between the two beams is confined to the end of the crystal where the pump is injected. This suggests that the effective length of the crystal is reduced and hence the stability of the steady solution is enhanced.

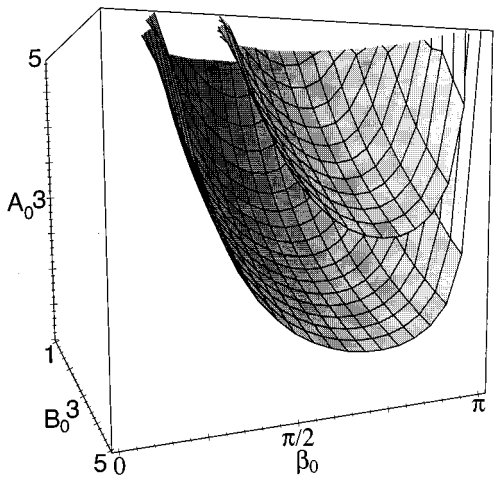

FIG. 7. The lower surface is the marginal stability surface for the steady solution in (β_0, B_0, A_0) space. The upper surface represents the locus of the next bifurcation points of the steady solution.

The linear stability analysis does not indicate whether the Hopf bifurcation is supercritical or subcritical, that is, whether the system changes smoothly to a temporally periodic solution or jumps discontinuously from the stationary solution to another state (see [19]). To investigate this issue and more generally determine the solution structure of the time periodic solutions that emerge at the bifurcation points, we have coupled the discretized time dependent nonlinear equations (39) to the software AUTO [20], which implements numerical continuation and bifurcation methods for systems of nonlinear ordinary differential equations. This has allowed us to track the steady solutions through the bifurcation points and confirmed the results obtained from the linear code described above. Further, we have used it to follow the temporally periodic solutions that emanate from the Hopf bifurcation points, assess their stability, and monitor for the appearance of further bifurcation points. From this information we were able to obtain bifurcation diagrams, see Fig. 9, which is typical of the results we obtained. We found that

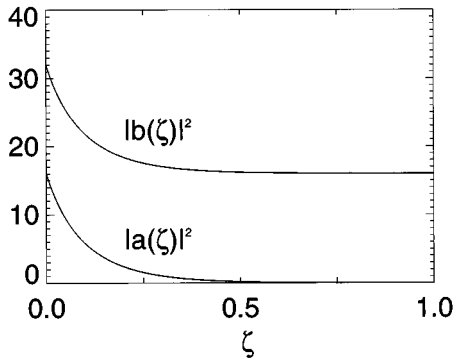

FIG. 8. A plot of the intensity of the two fields through the crystal for the case $A_0 = B_0 = 4$ and $\beta_0 = \pi$.

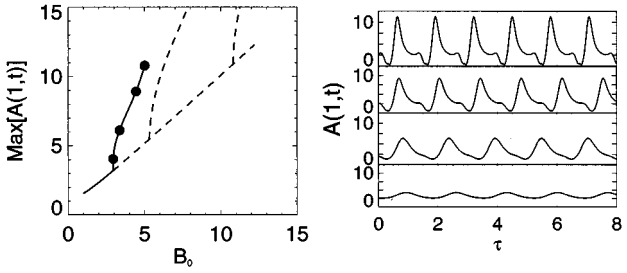

FIG. 9. Left: Bifurcation diagram of Eqs. (39) for $A_0=3$ and $\beta_0=\pi/2$. The bifurcation parameter is the input modulus of the backward field B_0. The solid (dashed) lines indicate stable (unstable) solutions. Right: plots of the four periodic orbits that correspond to the four dots on the stable Hopf branch. They are arranged in the same vertical order as the dots in the left-hand figure.

there are at least three supercritical Hopf bifurcations from the steady solution branch and that there are no bifurcation or limit points along time periodic branches. As a consequence the solution branch emanating from the first Hopf bifurcation is stable.

We found that as B_0 increases (for A_0 and β_0 fixed) the temporal period of the stable solution slowly decreases, see Fig. 10. It is interesting to note that the period of the oscillations is approximately equal to the crossing time through the crystal, although the physical mechanism for this is unclear. In contrast to the period, the amplitude of the oscillations depends strongly on the input intensity of the backward field with the peaks of the output field rapidly becoming sharper and more intense, see Fig. 9. Finally, in Fig. 11 we show a typical temporally periodic field configuration inside the crystal. The most noticeable feature is that the peaks of the pump beam are both sharper and more intense than those of the second harmonic. Moreover, the forward and backward fields are approximately in antiphase. This is reminiscent of a similar phenomenon that occurs when two beams counterpropagate in a defocusing Kerr medium [21]. In this

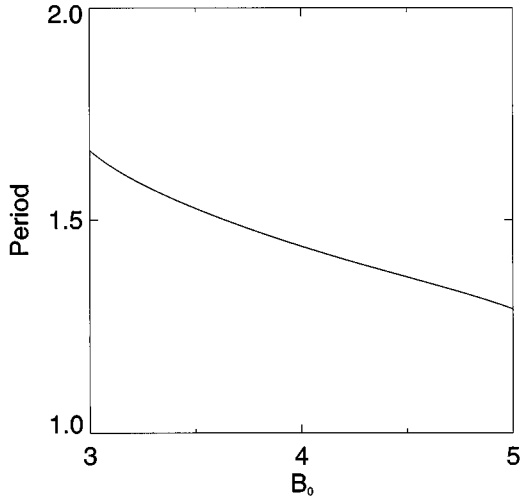

FIG. 10. Period of the stable periodic solution as a function of the backward field input modulus, B_0. Same parameter values as in Fig. 9, $A_0=3$, $\beta_0=\pi/2$.

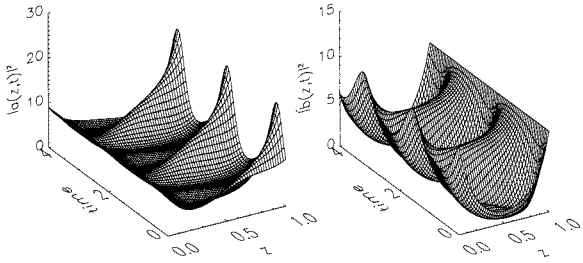

FIG. 11. Forward and backward field intensities across the crystal as a function of time. Parameter values $A_0=3.0$, $B_0=3.0$, and $\beta_0=\pi/2$.

case the two counterpropagating fields have a transverse dimension and they arrange themselves so that they are spatially in antiphase one with the other. In the case studied in this paper we do not allow for any transverse spatial dependence of the two fields: however, the two fields arrange themselves in order to be temporally out of phase.

V. CONCLUSIONS

We have shown that this device can be operated in two modes. At low input intensities it acts as a second-harmonic generator. It may also be switched into oscillatory mode by increasing the input intensity whereby a constant input beam is transformed into a pulsed beam on output. The period of the pulses is approximately the crossing time through the crystal. The oscillator is stable; increasing the input intensity changes the amplitude of the output but has little effect on its period. In this study we have not included transverse effects. Therefore it is possible that the system could become unstable to transverse modes and adopt a transversely inhomogeneous configuration in a similar way to that observed in a Kerr medium [21].

In the copropagating case, the state of the fields at any position depends entirely on propagation distance into the doubling medium. In backward phase-matching, however, the amplitude and phase of the fundamental and second-harmonic fields at any given position depend in a complex manner on the fields at every other point. This is because of

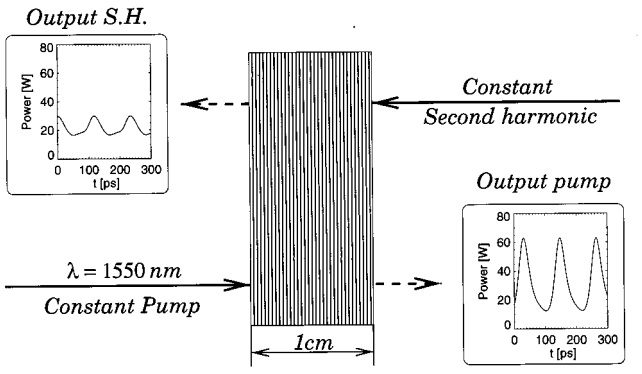

FIG. 12. A schematic diagram of the system comprising a lithium niobate crystal periodically poled with a pitch of 180 nm when the two input beams both have a power of 30 W and are in antiphase.

the distributed feedback nature of the interaction. The consequence is that self-consistent solutions are not necessarily always possible. If a solution is not self-consistent, oscillation or instability is likely to ensue. Backward phase-matched second-harmonic generators therefore display much richer physics than the more usual forward phase-matched devices.

The effects described in this paper could be observed experimentally in a lithium niobate waveguide, periodically poled for backward phase matching. For a 1 cm long interaction in a waveguide with mode area 10 μm^2, the power level of both the input pump and second-harmonic beams required to trigger the self-pulsing solution described in Fig. 9 at a pump wavelength of 1550 nm is roughly 30 W. The output of the device under these conditions is shown schematically in Fig. 12. The pitch required is of order $\lambda_{pump}/4n = 180$ nm, which lies beyond the current limits of electric field poling techniques. Higher order backward phase matching may be used, the effective interaction length going approximately as the reciprocal of the order. For a 10th-order backward interaction over 1 cm, therefore, the power level increases one hundred fold to 3 kW while the pitch increases to 1.8 μm, which is within reach of current techniques. However, these power levels may induce crystal damage and future realizations of this device must trade the available pitch to the allowable power. The unusual operating characteristics of this device may find uses in future parametric oscillators and amplifiers, in intracavity doubled waveguide lasers, and in passive mode locking.

[1] M.M. Fejer, G.A. Magel, D.H. Jundt, and R.L. Byer, IEEE J. Quantum. Electron. **QE-28**, 2631 (1992).
[2] Q. Chen and W.P. Risk, Electron. Lett. **30**, 1516 (1994).
[3] V. Pruneri, R. Koch, P.G. Kazansky, W.A. Clarkson, P.St.J. Russell, and D.C. Hanna, Opt. Lett. **20**, 2375 (1995).
[4] A. Balakrishnan, S. Sanders, S. Demars, J. Webjörn, D.W. Nam, R.J. Lang, D.G. Mehuys, R.G. Waarts, and D.F. Welch, Opt. Lett. **21**, 952 (1996).
[5] R. DeSalvo, D.J. Hagan, M. Sheik-Bahae, G. Stegeman, E. Stryland, and H. Vanherzeele, Opt. Lett. **17**, 28 (1992).
[6] L.A. Lugiato, C. Oldano, C. Fabre, E. Giacobino, and R.J. Horowicz, Il Nuovo Cimento **10**, 959 (1988).
[7] N.P. Pettiaux, R.-D. Li, and P. Mandel, Opt. Commun. **72**, 256 (1989).
[8] W.P. Risk, S.D. Lau, and M.A. McCord, IEEE Phot. Technol. Lett. **6**, 406 (1994).
[9] P.St.J. Russell, IEEE J. Quantum Electron. **27**, 830 (1991).
[10] P.St.J. Russell, Electron. Lett. **29**, 1228 (1993).
[11] S. Trillo and S. Wabnitz, Opt. Lett. **17**, 1572 (1992).
[12] S. Trillo, S. Wabnitz, R. Chisari, and G. Cappellini, Opt. Lett. **17**, 637 (1992).
[13] A.E. Kaplan, Opt. Lett. **18**, 1223 (1993).
[14] J.D. Cole, *Perturbation Methods in Applied Mathematics* (Blaisdell, Waltham, MA, 1968).
[15] A.H. Nayfeh, *Perturbation Methods*, 1st ed. (J. Wiley & Sons, Inc., New York, 1973).
[16] C. Canuto, M. Hussaini, A. Quarteroni, and T.A. Zang, *Spectral Methods in Fluid Dynamics* (Springer Verlag, New York, 1988).
[17] J.D. Hoffman, *Numerical Methods for Engineers and Scientists* (McGraw-Hill, New York, 1993).
[18] SLATEC Common Math Library, National Energy Software Center, Argonne National Laboratory, Argonne, IL, written by K.L. Hiebert, based on M.J.D. Powell, in *Numerical Methods for Nonlinear Algebraic Equations*, edited by P. Rabinowitz (Gordon and Breach, New York, 1970).
[19] P. Glendinning, *Stability, Instability and Chaos* (Cambridge University Press, Cambridge, 1994).
[20] E.J. Doedel, H.B. Keller, and J.P. Kernévez, Int. J. Bifurc. Chaos **1**, 693 (1991); **1**, 765 (1991).
[21] W.J. Firth, A. Fitzgerald, and C. Paré, J. Opt. Soc. Am. B **7**, 1087 (1990).